

Name : Subhankar Chakraborty

Roll Number : EE17B031

Reference : Convolutional Deblurring for Natural Imaging [1]



Department of Electrical Engineering

EE6110 Course Project

Instructor : Professor Srikrishna Bhashyam

December 27, 2020

I. ABSTRACT

This report investigates a novel design of image deblurring in the form of one-shot convolution filtering that can directly convolve with naturally blurred images for restoration. The problem of optical blurring is a common disadvantage to many imaging applications that suffer from optical imperfections. Despite numerous deconvolution methods that blindly estimate blurring in either inclusive or exclusive forms, they are practically challenging due to high computational cost and low image reconstruction quality. Both conditions of high accuracy and high speed are prerequisites for high-throughput imaging platforms in digital archiving. In such platforms, deblurring is required after image acquisition before being stored, previewed, or processed for high-level interpretation. Therefore, on-the-fly correction of such images is important to avoid possible time delays, mitigate computational expenses, and increase image perception quality. The reference paper [1] bridges this gap by synthesizing a deconvolution kernel as a linear combination of finite impulse response (FIR) even-derivative filters that can be directly convolved with blurry input images to boost the frequency fall-off of the point spread function (PSF) associated with the optical blur. It employs a Gaussian low-pass filter to decouple the image denoising problem for image edge deblurring. It also proposes a blind approach to estimate the PSF statistics for two Gaussian and Laplacian models that are common in many imaging pipelines. Most of the explanations in this report have been kept to a bare minimum for the sake of brevity. Complete proofs can be found in [1]. Deblurring experiments are performed on different naturally blurred datasets and compared to the results in [1]. Some of the results can be found here.

II. INTRODUCTION

Blurring in many imaging modalities is caused by inadequate optical configuration in image acquisition. In an imperfect optical system, a ray of light passing through the optical setup will spread over the image domain instead of converting to a single end point. This spreading effect is known as the point spread function (PSF) and characterizes the response (a.k.a impulse response) of the optical system [2, 3]. The corresponding observation model is usually expressed by a linear convolution

$$f_B(x) = f_L(x) * h_{PSF}(x) + \eta(x) \quad (1)$$

where f_B is the blurry image (image sampled), f_L is the latent image to be recovered, h_{PSF} is the impulse response of the point-spread function, and η is the noise contamination. The problem of deblurring (a.k.a deconvolution) refers to the restoration of the latent image from its blurry observation, which is inherently an ill-posed problem. When the PSF is given, this is known as the "*non-blind*" image deconvolution problem; otherwise, it is called the "*blind*" approach.

In general, a PSF suppresses high frequency content, i.e., sharp edges and this leads to blurry observations. It is known that no matter how well the system is in focus, including no motion artifacts, the aberrations are still barriers to generating high quality images. One approach to overcome this is to use sophisticated optical hardware, but, this is expensive. A more cost-effective solution is to integrate fast image-deblurring algorithms in order to maintain real-time image acquisition.

This method is divided into two main steps. First, a priori PSF model can be inferred by a scale-space analysis of the blurred image in the Fourier domain. After making an assumption about the frequency fall-off of natural images, the statistics of the PSF for two different models of the Gaussian and Laplacian as variants of the generalized Gaussian distribution are estimated. Second, a closed-form solution to the inverse PSF for deblurring is provided by fitting a series of polynomials in the frequency domain and then obtaining its equivalent representation in the spatial domain as a linear combination of FIR derivative filters. In doing so, ringing artifacts are avoided in the restored image while optimally preserving edge information on both fine and coarse resolutions.

III. CONTRIBUTIONS AND WORK DONE

A. Contributions from the authors

The paper makes the following technical contributions.

- Observes that the problems of image deblurring and denoising should be decoupled for reconstruction. It defines a dual spatial domain for image correction. It designs a closed-form solution of the deblurring problem as a linear combination of high-order FIR even-derivative filters.
- It adopts the generalized Gaussian distribution to model PSF blur and analyze its feasibility range for recovery using the proposed deblurring method.
- It formulates a new blind PSF estimation method using scale-space analysis in the Fourier domain considering two variants of Gaussian and Laplacian models for blind estimation of blur statistics.
- An adaptive tuning parameter is introduced based on the relative image entropy calculation to control the strength of deblurring

B. Work Done

The following work has been done by the student.

- Understanding the theory behind 1Shot-MaxPol [1]
- Evaluation of the proposed method, 1Shot-MaxPol on many natural blurred images. (The official MATLAB code can be found [here](#))
- Implementation of maximum local variation (MLV) metric [4] for no-reference sharpness quality assessment (NR-FQA). (The Python code can be found [here](#))
- Complexity analysis of the proposed 1Shot-MaxPol approach.

IV. PROPOSED DECOUPLED APPROACH

The paper proposes a new approach for symmetric PSF deblurring by correcting the fall-off of the high frequency band by means of frequency polynomial approximation. It constructs the dual representation in the spatial domain for inverse PSF deblurring in the form of one-shot convolution filters. The main approach here is to decouple denoising and blur correction by defining two separate convolutional filters in the dual spatial domain

$$h_D(x) = h_{PSF}^{-1}(x) * h_{Denoise}(x) \quad (2)$$

such that the convolution of the decoupled filter h_D in (2) with the blurry observed image, f_B , yields the latent approximation $\bar{f}_L(x) = h_D(x) * f_B(x)$. The merit of the design in (2) is the decoupling of the denoising and deblurring problems, enabling them to be individually addressed for recovery. One can separately apply a denoiser as a plug-in tool if the input image is perturbed with noise.

A. Inverse Deconvolution Kernel Design

The inverse filter in (2) is defined as the inverse Fourier transform of the inverse PSF response $h_{PSF}^{-1}(x) = \mathcal{F}^{-1}\{1/\hat{h}_{PSF}(\omega)\}$. However, as mentioned in [1], directly calculating the inverse Fourier will introduce Gibbs artifacts. To avoid this, a dual representation in both Fourier and spatial domains is defined by approximating the inverse PSF response in the Fourier domain by a series of frequency polynomials.

$$\frac{1}{\hat{h}_{PSF}(\omega)} \approx \sum_{n=0}^N \alpha_n \omega^{2n} \quad (3)$$

Only even polynomials are considered as the symmetry of the PSF ensures that the inverse response will be an even function. The unknown coefficients are determined by fitting the inverse PSF response to polynomial series up to certain frequency range.

$$\min_{\alpha_n} \left\| \frac{1}{\hat{h}_{PSF}(\omega)} - \sum_{n=0}^N \alpha_n \omega^{2n} \right\|_2, \quad \omega \in [0, \omega_T], \quad (4)$$

where the range ω_T is tweaked to avoid fitting instabilities. The numerical solution to the fitting problem in (4) is obtained by solving a least-squares problem in [5]. From (4), the equivalent representation in the spatial domain can be represented as

$$h_{PSF}^{-1}(x) \approx \delta(x) + \sum_{n=1}^N \alpha_n (-1)^n \frac{\partial^{2n}}{\partial x^{2n}} \quad (5)$$

The continuous derivative operators in (5) can be numerically approximated using Finite Impulse Response (FIR) convolution filters

$$h_{PSF}^{-1}[k] = \delta[k] + D[k] \quad (6)$$

where $D[k] = \sum_{n=1}^N \alpha_n (-1)^n d^{2n}[k]$ is the associated deblurring kernel. $d^{2n}[k]$ is the discrete time approximation to the $2n^{th}$ order derivative in the continuous domain. More details and implementation results can be found in [1].

B. Decoupled Smoothing Filter

The whole idea of decoupled design in (2) is to balance the amplitude fall-off of high frequency components caused by the PSF kernel. Ideally speaking, if no denoising/cut-off is considered, all of the frequency domain will be deconvolved according to the inverse kernel response. However, such full correction should be avoided due to noise contamination in real applications. Once the image is deconvolved by an inverse filter, similar symmetric blur kernels with less blur scale than that considered for deconvolution are applied (convolved) for denoising. This guarantees that the fall-off of the high frequency amplitude will be balanced between noise cancellation and amplifying meaningful edge information. More details and examples can be found in [1].

C. Two Dimensional Deblurring Framework

For imaging applications, the discussions in the previous section must be extended to two dimensions (2D). Let $f(x, y) \in \mathbf{R}^{N_1 \times N_2}$ represent the image in the 2D domain, with N_1 and N_2 being the number of discrete pixels along the vertical and horizontal axes, respectively. The PSF blur in many optical imaging systems is considered to be rotationally symmetric - the associated blurring operator is identical in any arbitrary rotational angle i.e. $h_{PSF}(r, \theta) = h_{PSF}(r)$. In general, it is also assumed that the blur operator is independently applied in both dimensions (separable mode). So the linear model in (1) can be revised to

$$f_B(x, y) = f_L(x, y) * h_{PSF}(x) * h_{PSF}(y) + \eta(x, y) \quad (7)$$

The corresponding deblurring kernels in both directions are designed by means of the approximation method in the previous section and applied to the blurry image for reconstruction

$$f_R(x, y) = f_B(x, y) * h_D(x) * h_D(y) \quad (8)$$

The energy level of the blurring kernel is usually unknown *a priori* for natural imaging problems. A tuning parameter $\gamma \in [0, 1]$ is defined to control the significance of the deconvolution level.

$$f_R(x, y) = f_B(x, y) + \gamma \nabla_D f_B(x, y) \quad (9)$$

where $\nabla_D f_B(x, y) = f_B(x, y) * [D_x + D_y + D_{xy}]$ gives the reconstructed images and $D_{xy} = D_x * D_y$ is the crossed deconvolution operator independently applied to the horizontal and vertical axes. More details can be found in [1].

D. Adaptive Level Tuning

The significance level γ is calculated as the relative ratio of two image entropies.

$$\gamma \triangleq \frac{E(f_B)}{E(\nabla_D f_B) + T} \quad (10)$$

where $E(I)$ represents the entropy of an input image calculated using the image histogram. More details can be found in [1].

V. BLUR MODELING AND ESTIMATION

A. Modeling Blur by Generalized Gaussian (GG)

The generalized Gaussian (GG) distribution, introduced in [6], is given by

$$h_{GG}(x) = \frac{1}{2\Gamma(1+1/\beta)A(\beta,\sigma)} \exp - \left| \frac{x}{A(\beta,\sigma)} \right|^{\beta} \quad (11)$$

where β defines the shape of the distribution function, $A(\beta,\sigma) = (\sigma^2 \Gamma(1/\beta) \Gamma(3/\beta))^{1/2}$ is the scaling parameter and $\Gamma(.)$ is the Gamma function, i.e., $\Gamma(z) = \int_0^\infty e^{-t} t^{z-1} dt$. The GG model is used in several imaging applications to model static blur in natural imaging, such as atmospheric turbulence and optical aberrations. A common approach is to employ such kernels in a non-blind fashion for image deconvolution. The shape and the scale are the two different characteristics that fit different blur applications. Refer to [1] for more information on the GG.

B. Blind PSF Estimation

In this section a blind approach to estimate the blur level of the PSF kernel from naturally blurred images is introduced. This approach relies on image scale-space analysis using two different scales that are the originally sampled image $f_B(x,y)$ and its down-sampled version $f_B(sx,sy)$ for $s > 1$. This scale is reversed in the Fourier domain, i.e. $\hat{f}_B(\omega x/s, \omega y/s)$, where the coordinates are transferred from Cartesian to polar $(\omega x, \omega y) \rightarrow (r, \theta)$ to obtain $\hat{f}_B(r/s, \theta)$. The blur image is integrated along a closed circle to calculate its radial spectrum and the terms are expanded using the linear convolution model in (1) which gives

$$\int_0^{2\pi} \hat{f}_B(r/s, \theta) d\theta \approx \int_0^{2\pi} \hat{f}_L(r/s, \theta) \hat{h}(r/s, \theta) d\theta + \hat{\eta} d\theta \quad (12)$$

The integral in (12) calculates the radial spectrum of the input image along the radial ring. Natural images (without blur) usually follow a decay spectrum of $\hat{f}_L \approx 1/r$ [7–9]. Furthermore, the noise contamination is assumed to be additive white Gaussian noise (AWGN). Substituting these assumptions into the expansion in (12) gives

$$\int_0^{2\pi} \hat{f}_B(r/s, \theta) d\theta \approx \int_0^{2\pi} \frac{s}{r} \hat{h}(r/s, \theta) d\theta + c \quad (13)$$

where $c \propto SNR^{-1}$ is proportional to the inverse signal-to-noise-ratio (SNR) level of the sample measurements. For good quality images, this coefficient is negligible ($c \rightarrow 0$). Next, a ratio spectrum of two different scales of original and subsampled domains is defined:

$$R(r) = \frac{\int_0^{2\pi} \hat{f}_B(r, \theta) d\theta}{\int_0^{2\pi} \hat{f}_B(r/s, \theta) d\theta} \approx \frac{\int_0^{2\pi} \hat{h}(r, \theta) d\theta + cr}{\int_0^{2\pi} \frac{s}{r} \hat{h}(r/s, \theta) d\theta + cr} \quad (14)$$

The right-hand-side (RHS) of equation (14) is used to fit a certain blur model as a prior knowledge of the equation, where the data fidelity term is provided by approximating the ratio $R(r)$ using two radial spectra of different image scales. Calculation of the radial spectrum as well as two different cases of generalized Gaussian for blur scale estimation, Gaussian ($\beta = 2$) and Laplacian ($\beta = 1$) can be found in [1]. In both blur models (Gaussian/Laplacian), the unknown parameters scale α and noise level c' are obtained by solving a linear least square problem from [5].

VI. EVALUATION AND EXPERIMENTS

A. Maximum Local Variation

In this section, the MLV metric is described. It is a fast metric for no-reference sharpness quality assessment (NR-FQA). It was introduced in [4], where high values indicate better focus resolution and lower values indicate the opposite.

1) *Definition*: For a grayscale image I with pixel value at coordinates (i, j) represented by $I_{i,j}$, the MLV at coordinates (i, j) , denoted by $\psi(I_{i,j})$, is defined as

$$\begin{aligned} \psi(I_{i,j}) = \max |I_{i,j} - I_{x,y}| \\ x \in \{i-1, i, i+1\} \\ y \in \{j-1, j, j+1\} \end{aligned} \quad (15)$$

Basically, the maximum value of the absolute difference between a pixel and its 8-neighbors is considered the MLV at that pixel. In the gray scale images, MLV changes in the range of 0–255. The value of 0 means there is no variation between a pixel and its 8-neighbors while the value of 255 shows the highest variation between the pixel and its 8-neighbors. An illustration can be found in [4]. Often the MLV values for grayscale images are normalized to be in the range [0,1].

2) *MLV Map generation*: Given a colour image of the shape $M \times N$, it is first converted into a grayscale image. Then, for each pixel $I_{i,j}$, its MLV value is calculated using its 8-neighbors as defined in (15). These values are then used to generate the MLV Map, $\Psi(I)$ given by

$$\Psi(I) = \begin{bmatrix} \psi(I_{1,1}) & \dots & \psi(I_{1,N}) \\ \vdots & \ddots & \vdots \\ \psi(I_{M,1}) & \dots & \psi(I_{M,N}) \end{bmatrix} \quad (16)$$

An image with its corresponding MLV Map is shown in figure 1.

3) *Weighted MLV Map*: The tail end of the distribution discriminates the blur degree differences (see [4]). The pixels with large MLV have more influences in the sharpness assessment. By changing the distribution in such a way that the tail part becomes heavy, the distribution can be used to evaluate the sharpness more effectively. This can be done by assigning higher weights to the larger MLV

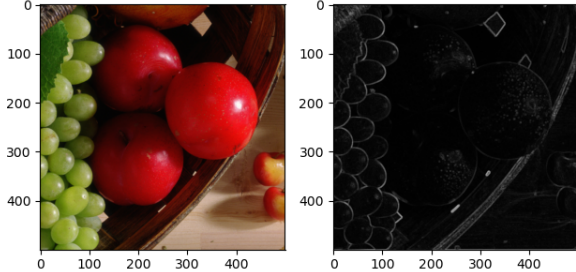


Fig. 1: Image and its MLV Map

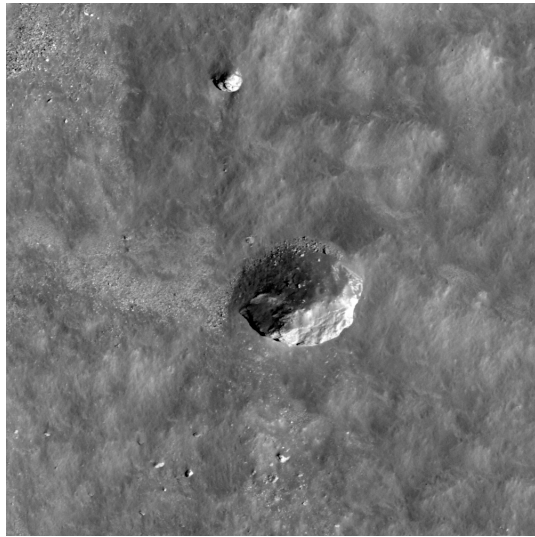


Fig. 2: Image of the Moon surface from NASA Archives

pixels by generating the weighted MLV map $\Psi_w(I)$ below

$$\Psi_w(I) = \begin{bmatrix} w_{1,1}\psi(I_{1,1}) & \dots & w_{1,N}\psi(I_{1,N}) \\ \vdots & \ddots & \vdots \\ w_{M,1}\psi(I_{M,1}) & \dots & w_{M,N}\psi(I_{M,N}) \end{bmatrix} \quad (17)$$

where weights $w_{i,j}$ are defined using exponential function $w_{i,j} = e^{\eta_{i,j}}$ and $\eta_{i,j}$ is the rank of $\Psi(I_{i,j})$ when sorted in ascending order from 0 to 1. Finally, standard deviation of the weighted MLV distribution is used as the metric to measure sharpness calculated using the moment matching method in [10].

B. Natural Image Database

A brief description of the different natural image databases used for the evaluation is provided here. Experiments could not be run on the Hyperspectral Imaging Camera and Haze Images datasets as those were not open source and collected by the authors of [1] themselves.



Fig. 3: Image from the McMaster dataset

1) *NASA Archives*: Instead of LROC, 25 images of the Moon's surface are collected from the NASA archives (available [here](#)). One such sample is shown in figure 2.

2) *McMaster Images*: The McMaster database is constructed with true RGB color from Kodak film. The database contains 18 image patches of size 500×500 pixels and are cropped from eight image scenes. One of the images in the dataset is shown in figure 3. The dataset can be downloaded [here](#).

3) *NIR-RGB Scene Dataset*: Images in this dataset are captured by Nikon D90 and Canon T1i cameras using both visible and near infrared (NIR) filters with 750nm cut-off between the two filters. Images are processed after image acquisition using white balance correction. Both NIR and RGB images are registered using SIFT features and the final images are re-sampled. The dataset can be downloaded [here](#). A sample is shown in figure 4a and 4b.

C. Empirical Performance Evaluation

In this section, the sharpness of each image in a dataset is calculated using the MLV metric. A box plot of these sharpness values is generated for each dataset. The boxplot is generated for the original images in the dataset as well as the ones deblurred using the Gaussian and Laplacian kernel. The plots are shown in figures 5, 6, 7, and 8.

A clear trend is that modeling the PSF as a Gaussian performs better than modeling the PSF as a Laplacian. The MLV code used for evaluation can be found [here](#).

D. Qualitative results

Qualitative results are shown in figures 9 and 10 using both the Gaussian and Laplacian kernels. A cropped section of the original as well as the deblurred image is shown to help notice the difference in image sharpness in the regions with sharp edges.



(a) RGB



(b) NIR

Fig. 4: RGB and corresponding NIR image of a forest scene

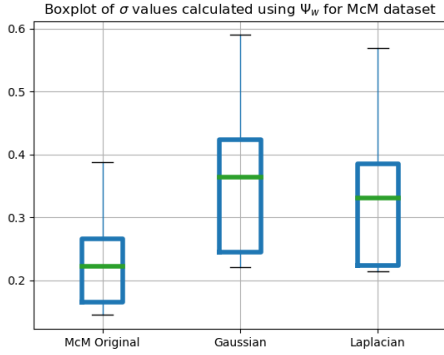


Fig. 5: Performance on McM dataset

E. Complexity Analysis

In this section the complexity of the proposed 1Shot-MaxPol method is evaluated. It is important to note that the time taken for the proposed blind PSF estimation is not counted. All computations in this section were performed

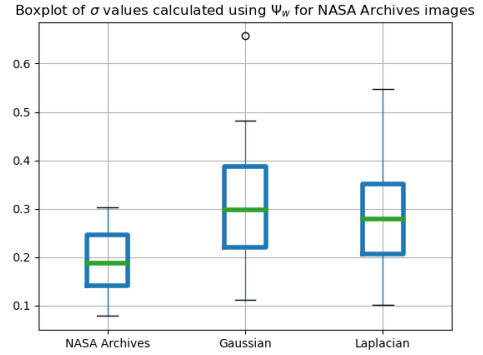


Fig. 6: Performance on NASA Archives

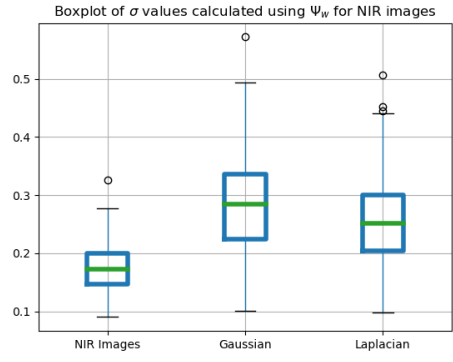


Fig. 7: Performance on NIR images

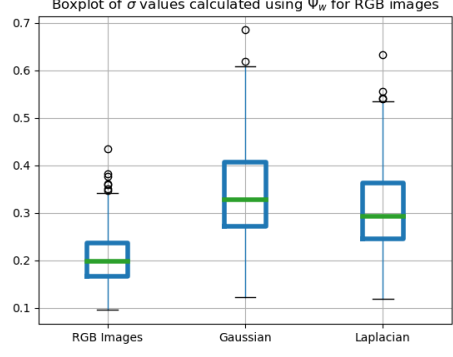


Fig. 8: Performance on RGB images

on an Intel i7-7700HQ laptop running Pop!_OS 20.10. The MATLAB version used is R2019b. The proposed method is run on one image each of size $N \times N$ with $N \in \{64, 128, 256, 512, 1024, 2048, 4096\}$ 11 times. The median of time taken in the 11 runs is considered. This process is repeated for each image size. The results can be seen in figure 11.

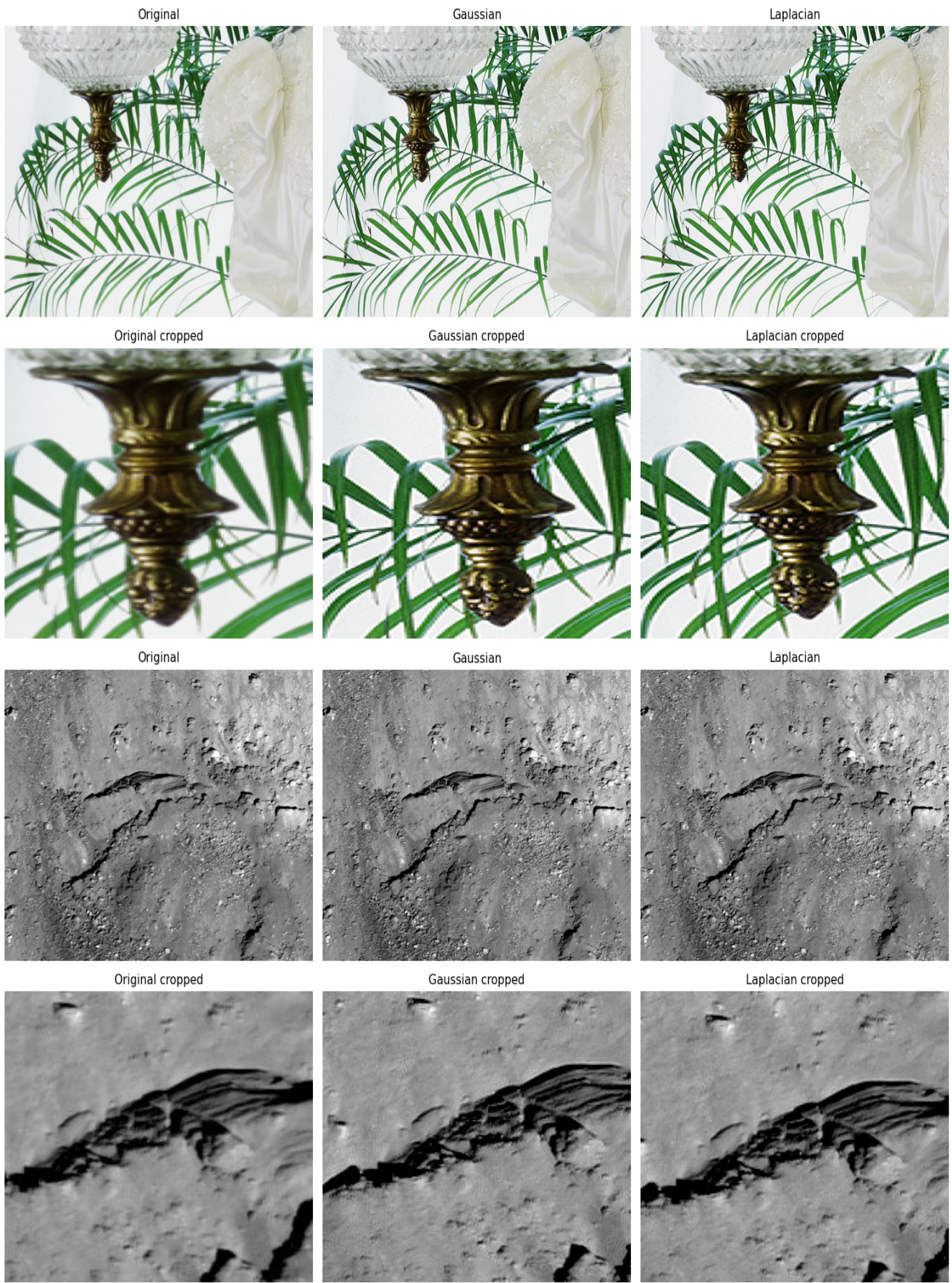


Fig. 9: Qualitative results from the McMaster dataset and NASA Archives. The first two rows correspond to an image from the McMaster dataset deblurred with both the Gaussian and Laplacian kernel and a zoomed in section of each of it. The next two rows contain the same for the NASA image.

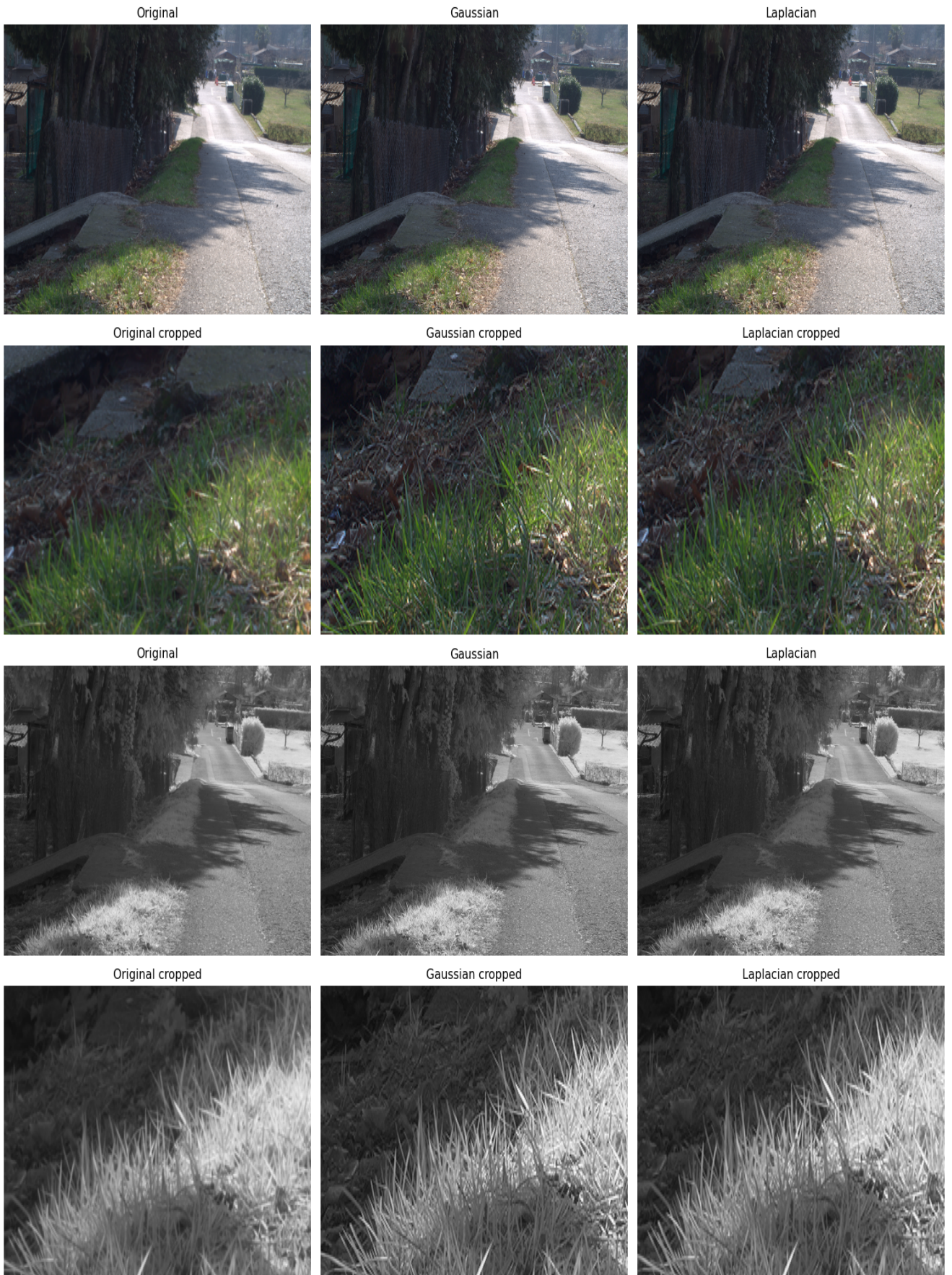


Fig. 10: Qualitative results from the NIR-RGB Scene dataset. The first two rows correspond to an RGB image from the dataset deblurred with both the Gaussian and Laplacian kernel and a zoomed in section of each of it. The next two rows contain the same for its corresponding NIR image.

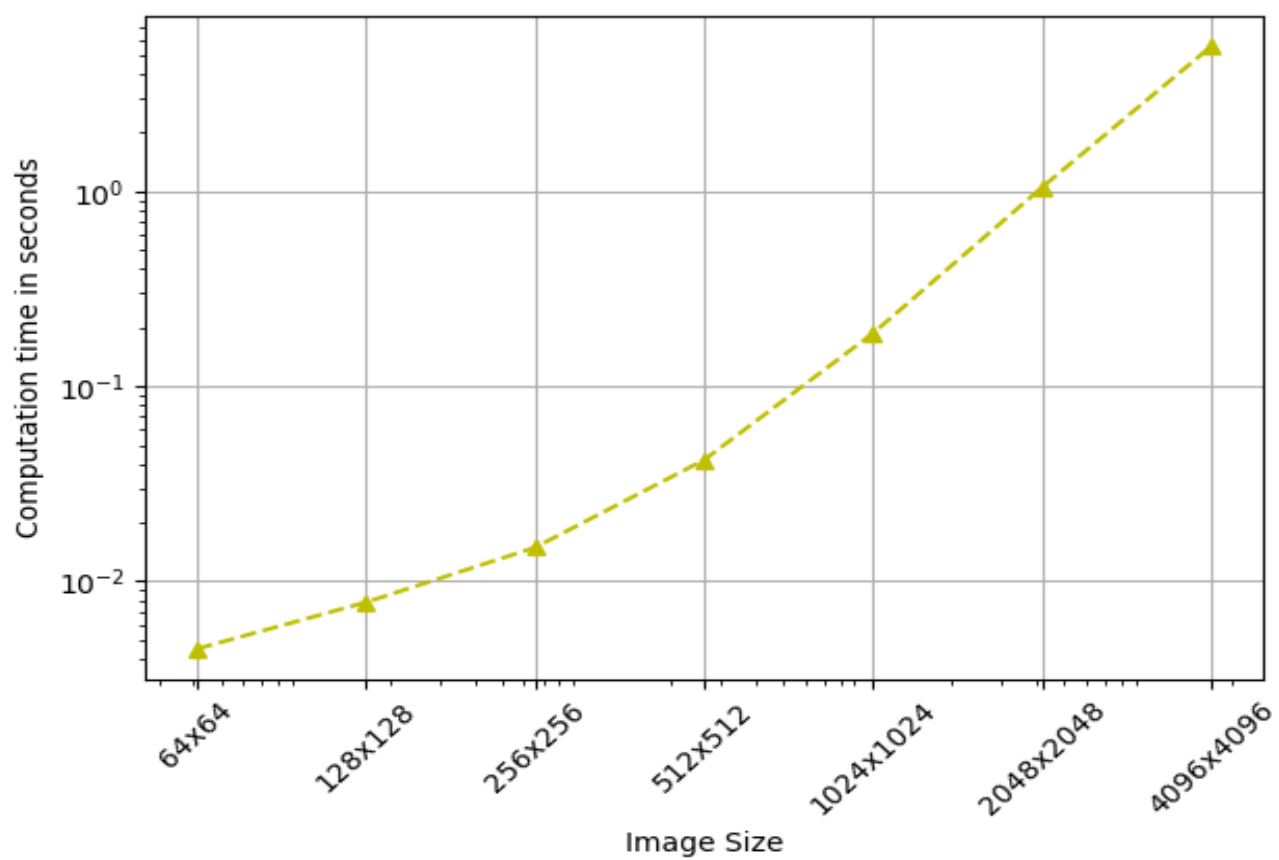


Fig. 11: Complexity analysis

REFERENCES

- [1] Mahdi S Hosseini and Konstantinos N Plataniotis. Convolutional deblurring for natural imaging. *IEEE Transactions on Image Processing*, 29:250–264, 2019.
- [2] Neel Joshi, Richard Szeliski, and David J Kriegman. Psf estimation using sharp edge prediction. In *2008 IEEE Conference on Computer Vision and Pattern Recognition*, pages 1–8. IEEE, 2008.
- [3] H Ernst Keller. Objective lenses for confocal microscopy. In *Handbook of biological confocal microscopy*, pages 145–161. Springer, 2006.
- [4] Khosro Bahrami and Alex C Kot. A fast approach for no-reference image sharpness assessment based on maximum local variation. *IEEE Signal Processing Letters*, 21(6):751–755, 2014.
- [5] Carl T Kelley. *Iterative methods for optimization*. SIAM, 1999.
- [6] M Th Subbotin. On the law of frequency of error. *Mathematical collection*, 31(2):296–301, 1923.
- [7] David J Field. Relations between the statistics of natural images and the response properties of cortical cells. *Josa a*, 4(12):2379–2394, 1987.
- [8] Nuala Brady and David J Field. What’s constant in contrast constancy? the effects of scaling on the perceived contrast of bandpass patterns. *Vision research*, 35(6):739–756, 1995.
- [9] David J Field and Nuala Brady. Visual sensitivity, blur and the sources of variability in the amplitude spectra of natural scenes. *Vision research*, 37(23):3367–3383, 1997.
- [10] Karnran Sharifi and Alberto Leon-Garcia. Estimation of shape parameter for generalized gaussian distributions in subband decompositions of video. *IEEE Transactions on Circuits and Systems for Video Technology*, 5(1):52–56, 1995.